Received: 11 November 2021 | Revised: 31 May 2022 | Accepted: 1 June 2022

DOI: 10.1002/fld.5122

RESEARCH ARTICLE

WILEY

A splitting method for the numerical simulation of free surface flows with sediment deposition and resuspension

Arwa Mrad[1,2] | **Alexandre Caboussat**[2] | **Marco Picasso**[1]

[1]Institute of Mathematics, Ecole polytechnique fédérale de Lausanne, Lausanne, Switzerland

[2]Geneva School of Business Administration, University of Applied Sciences and Arts Western Switzerland (HES-SO), Carouge, Switzerland

Correspondence
Alexandre Caboussat, Geneva School of Business Administration, University of Applied Sciences and Arts Western Switzerland (HES-SO), Rue de la Tambourine 17, 1227 Carouge, Switzerland.
Email: alexandre.caboussat@hesge.ch

Funding information
Swiss Government Excellence Scholarship; Grant/Award Number: ANR-15-CE01-0013

Abstract

We present a numerical model for the simulation of 3D sediment transport in a Newtonian flow with free surfaces. The Navier–Stokes equations are coupled with the transport, deposition, and resuspension of the particle concentrations, and a volume-of-fluid approach to track the free surface between water and air. The numerical method relies on operator splitting to decouple advection and diffusion phenomena, and a two-grid method. An appropriate combination of characteristics, finite volumes, and finite elements methods is advocated. The numerical model is validated through comparisons with numerical experiments, sediment flushing, shear flow erosion, and the formation of dunes.

KEYWORDS

free surface flow, operator splitting, particle flow, sediment resuspension, sediment transport

1 | INTRODUCTION

Sediment transport occurs in many systems such as dam retention basins, rivers, lakes, or shores. The accumulation of sediments can have major negative sociological, economic, and environmental effects on water resources management. Sedimentation can alter reservoir routing, complicate the management of flood inflow and reduce the discharge capacity. This causes structural damages, affects operations efficiency, and even influences hydraulic energy production.[1] Quantifying sediment transport is therefore very important for hydraulic and coastal engineering.

Since sedimentation is a complex physical phenomenon, it has been investigated and simulated using several different approaches. A first widespread model is to treat the liquid and the sediment as two distinct phases and is referred to as the two-phase model. Lagrangian–Lagrangian models (also called discrete particle models) depicts both phases as disperse. The motion of the liquid phase may be described with fully Lagrangian SPH (smoothed particle hydrodynamics)[2-5] or MPS (moving particle semi-implicit).[6,7] However, Lagrangian–Lagrangian models can be computationally expensive. Eulerian–Lagrangian models (also referred to as particle-laden flows) treat the water phase as a continuum while tracking the movement of each sediment particle at the microscopic scale.[8-10] Various Eulerian–Lagrangian models exist, including the arbitrary Lagrangian–Eulerian method,[11] the lattice Boltzmann method,[12] or the fictitious domain method.[13] Finally

Eulerian–Eulerian approaches consider both phases (liquid and sediment) as continuous phases.[14-18] They can be further classified into mixed or separated-fluid approaches.[18-21] Various methods[22-24] have been studied to model the relative motion between the fluid and the sediment, but most of the formula proposed are either valid only for the gravity-induced settling or only in limited ranges of concentrations or grain sizes.

We present here a novel numerical method for the simulation of sediment dynamics together with free surfaces. The novelty lies in the hybrid discretization of the various operators in an operator splitting framework, mixing finite elements, finite volumes, and finite differences. The model we propose is a three-dimensional mixed-fluid model with an Eulerian–Eulerian approach, for the modeling of sediments in a Newtonian fluid with free surfaces. The objective is to establish a general mixture model with a broad range of applications, by introducing deposition and resuspension effects. Our miscible model is based on a sediment concentration with a single momentum balance for the mixture (sediments and liquid). It is built to have a continuous concentration taking into account dilute and non-dilute situations. In previous works,[25] mass conservation of the sediments was introduced to take into account sediment transport and deposition. Jet erosion was successfully reproduced but comparison to sediment flushing showed discrepancies, indicating that the resuspension effects were necessary. The goal of this work is therefore to introduce resuspension effects in the model.

The numerical method relies on a splitting algorithm and a two-grid method. It has successfully been used to simulate Newtonian,[26] and viscoelastic fluid flows.[27] The time-splitting algorithm is used to decouple diffusion, and advection. The two-grid method consists of two meshes: a coarse non-structured finite element mesh, and a finer structured Cartesian mesh that aims at improving the accuracy of the approximation of the free-surface. A volume-of-fluid (VOF)[28,29] is used to track free surfaces. A Simple Line Interface Calculation (SLIC) algorithm is added[30] to reduce numerical diffusion. Extending the splitting approach, we decompose the sedimentation equation into transport, deposition, and resuspension operators. This allows us to use a mix of finite elements, characteristics method, finite differences, and finite volumes based on a Riemann solver with the Godunov scheme.[31]

Such mixed methods are also called *hybrid* in the literature. Several examples for coupled problems in fluid mechanics are using the same type of splitting approach.[32-34] In particular, Busto et al.[32] include a similar model for species transport, in addition to a turbulence model. Hyperbolic operators are discretized with a finite volume method. The corresponding mesh is defined by duality, unlike the space discretization approach advocated here.

Several numerical experiments validate the mathematical model for a large range of applications. This article is structured as follows. In Section 2, we describe the mathematical model for coupling the evolution of a Newtonian fluid with free surfaces with sediment transport. Sections 3 and 4 detail respectively the time and space discretizations. The results of numerical experiments for various test cases involving flushing, vertical and horizontal scouring effects are presented in Section 5.

2 | MATHEMATICAL MODEL

Let $\Lambda \in \mathbb{R}^3$ be a cavity containing the fluid (liquid and sediments) and the ambient air, and let $T > 0$ be the final time of the simulation. The multiphysics model we consider reads as follows.

First, a volume-of-fluid (VOF)[28,29] method is used to track the fluid. The tracking is achieved through the characteristic function of the liquid $\varphi : \Lambda \times (0,T) \to \{0,1\}$ (the volume fraction of liquid). Then Q_T, the space-time domain containing the liquid is defined by $Q_T = \{(\mathbf{x},t) \in \Lambda \times (0,T) : \varphi(\mathbf{x},t) = 1\}$. The velocity field $\mathbf{v} : Q_T \to \mathbb{R}^3$ and the pressure field $p : Q_T \to \mathbb{R}$ satisfy the time-dependent, incompressible Navier–Stokes equations, with variable density and viscosity coefficients, and modified by an additional Darcy-like reaction term.[35,36] Finally, the sediment concentration $f_s : Q_T \to [0, f_{s_{CR}}]$ where $f_{s_{CR}}$ is the maximal sediment solid fraction, satisfies a nonlinear conservation law.

More precisely, the presence rate f_s is a percentage of solid sediment in a given volume. The critical value $f_{s_{CR}} < 1$ (i.e., the solid fraction of the packed sediments) is essentially related to grains' size and shape. In this work, the sediment particles are assumed to be spherical and fully immersed in the liquid (wet sediments), and $f_{s_{CR}} = 0.61$. A 2D sketch of the situation is illustrated in Figure 1.

In order to describe the kinematics of the free surface, the characteristics function φ (the volume fraction of liquid) satisfies (in a weak sense):

$$\frac{\partial \varphi}{\partial t} + \mathbf{v} \cdot \nabla \varphi = 0 \qquad \text{in } \Lambda \times (0,T). \tag{1}$$

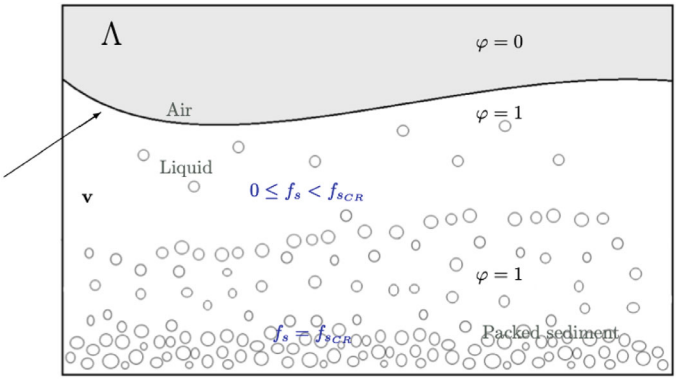

FIGURE 1 2D sketch of the computational domain for sedimentation. The cavity Λ contains the air and the liquid, separated by a free surface. The liquid domain is described by its characteristic function φ (the volume fraction of liquid). The velocity $\mathbf{v}$, pressure and sediment concentration f_s are defined in the liquid region only. The sediment concentration f_s ranges between 0 and a maximum value $f_{s_{CR}}$. [Colour figure can be viewed at wileyonlinelibrary.com]

This equation translates the fact that the fluid particles move at velocity $\mathbf{v}$. More precisely, $\mathbf{v}(\mathbf{X}(t), t) = \mathbf{v}(\mathbf{X}(0), 0)$, where $\mathbf{X}(t)$ is the trajectory of a fluid particle starting from $\mathbf{X}(0)$ at time $t = 0$, thus $\mathbf{X}'(t) = \mathbf{v}(\mathbf{X}(t), t)$ and $\mathbf{v}$ is not needed in the surrounding air. The characteristic function φ is given at initial time. Whenever liquid is entering the cavity Ω, we set $\varphi = 1$.

We assume that the liquid mixture velocity $\mathbf{v}$ and pressure p satisfy the Navier–Stokes equations in Q_T:

$$\rho_m(f_s)\left(\frac{\partial \mathbf{v}}{\partial t} + (\mathbf{v}\cdot\nabla)\,\mathbf{v}\right) - 2\nabla\cdot(\mu_m(f_s)\mathbf{D}(\mathbf{v})) + \alpha_m(f_s)\mathbf{v} + \nabla p = \rho_m(f_s)\mathbf{g}, \tag{2}$$

$$\nabla\cdot\mathbf{v} = 0. \tag{3}$$

Here $\mathbf{D}(\mathbf{v}) = 1/2(\nabla\mathbf{v} + \nabla\mathbf{v}^T)$ is the symmetric deformation tensor, and $\mathbf{g}$ denotes the gravity field. The density ρ_m is given by:

$$\rho_m = \rho_m(f_s) = \rho_l(1 - f_s) + \rho_s f_s, \tag{4}$$

where ρ_l (resp. ρ_s) is the fluid density (resp. the sediment density). The viscosity μ_m is the apparent viscosity of the fluid with the suspended particles. The model for particle flows introduced in Reference 37, is used here and reads:

$$\mu_m(f_s) = \begin{cases} \mu_l\left(1 - \frac{f_s}{f_{s_{CR}}}\right)^{-2.5 f_{s_{CR}}}, & \text{if } f_s < f_{s_{CO}}, \\ \mu_l\left(1 - \frac{f_{s_{CO}}}{f_{s_{CR}}}\right)^{-2.5 f_{s_{CR}}}, & \text{otherwise}, \end{cases} \tag{5}$$

where μ_l is the Newtonian dynamic viscosity of the fluid and $f_{s_{CO}}$ is a cohesion threshold parameter to be calibrated. The choice of (5) is validated in the literature for small values of f_s.[37] The Navier–Stokes equations (2) and (3) contain an additional Brinkman term, using Carman–Kozeny empirical law, to represent the coupling with Darcy flow in porous media.[38] The reaction coefficient $\alpha_m = \alpha_m(f_s)$ in (2) is given by:

$$\alpha_m(f_s) = K\frac{\mu_l f_s^2}{d_*^2(f_{s_{CR}} - f_s + \varepsilon)^3}, \tag{6}$$

where $K > 0$ and $\varepsilon > 0$ are constants to be calibrated and d_* is the mean sediment particle diameter. Note that the numerical parameter ε in (6) avoids a division by zero when $f_s = f_{s_{CR}}$. The Navier–Stokes equations (2) and (3) are completed with initial and boundary conditions: slip, no-slip, or inflow boundary conditions on $\partial\Lambda$.

Surface tension effects on the liquid–gas interface are not taken into account, and the ambient air is treated as vacuum, and thus has no influence on the fluid. The boundary conditions on the liquid–air interface are then given by the no-force boundary condition:

$$-p\mathbf{n} + 2\mu_m(f_s)\mathbf{D}(\mathbf{v})\mathbf{n} = \mathbf{0}, \tag{7}$$

with $\mathbf{n}$ the external normal vector to the liquid–air interface. The sediment concentration f_s satisfies the nonlinear equation:

$$\frac{\partial f_s}{\partial t} + \nabla \cdot \left(F_l(f_s) \left(k v_{stokes} \frac{\mathbf{g}}{\|\mathbf{g}\|} - A(f_s, \mathbf{v}) \nabla f_s \right) \right) = 0, \tag{8}$$

with

$$F_l(f_s) := f_s \left(1 - \frac{f_s}{f_{s_{CR}}} \right).$$

The first flux of (8) , $F_l(f_s) \left(k v_{stokes} \frac{\mathbf{g}}{\|\mathbf{g}\|} \right)$, is a parabolic *deposition* flux, where k is a positive parameter independant from f_s and v_{Stokes} is the maximal sediment velocity given by the Stokes' law:

$$v_{Stokes} = \frac{{d_*}^2 \|\mathbf{g}\| (\rho_s - \rho_l)}{18 \mu_l}.$$

The deposition flux vanishes when $f_s = 0$ (no sediments) and when $f_s = f_{s_{CR}}$, (packed sediments), see, for example, Reference 39, and the maximum principle (i.e., $f_s \in [0, f_{s_{CR}}]$) holds.[40]

The second flux of (8), $-F_l(f_s)\,(A(f_s, \mathbf{v})\nabla f_s)$, is a *resuspension* flux, where, following Reference 41, $A(f_s, \mathbf{v})$ is given by:

$$A(f_s, \mathbf{v}) = K_r \left(\frac{\tau(f_s, \mathbf{v}) - \tau_{CR}}{\tau_{CR}} \right)_+,$$

where K_r is the resuspension constant (m^2/s), $(v)_+ = \max(v, 0)$, $\tau(f_s, \mathbf{v})$ (N/m^2) is given by the tangential part of the stress tensor:

$$\tau(f_s, \mathbf{v}) = 2\mu_m(f_s) \| \mathbf{D}(\mathbf{v})\mathbf{n}(f_s) - (\mathbf{D}(\mathbf{v})\mathbf{n}(f_s) \cdot \mathbf{n}(f_s))\mathbf{n}(f_s) \|, \tag{9}$$

where $\mathbf{n}(f_s) = \frac{\nabla f_s}{\|\nabla f_s\|}$ for $\nabla f_s \neq \mathbf{0}$. If $\nabla f_s = \mathbf{0}$, we set $\tau(f_s, \mathbf{v}) = 0$. Equation (8) is thus a *degenerate parabolic equation*. The resuspension occurs only when there is enough shear on the sediment bedload that is, when $\tau(f_s, \mathbf{v})$ is above a given critical shear value τ_{CR}. We consider two configurations: first a constant critical shear $\tau_{CR} \in [0.02, 0.5]$,[42] but also the so-called Shields shear[43] defined as:

$$\tau_{CR}(f_s, \mathbf{v}) = \theta(f_s, \mathbf{v})\,(\rho_s - \rho_l)\,\|\mathbf{g}\| d_*,$$

where

$$\theta(f_s, \mathbf{v}) = \begin{cases} 0.010595 \ln(Re_*) + \frac{0.110476}{Re_*} + 0.0027197 & \text{for} \quad Re_* \leq 500, \\ 0.068 & \text{for} \quad Re_* > 500. \end{cases}$$

Here the shear Reynolds number $Re_* = Re_*(f_s, \mathbf{v})$[44,45] is defined by:

$$Re_*(f_s, \mathbf{v}) = \frac{u_*(f_s, \mathbf{v}) d_*}{\nu_l}, \quad \text{where} \quad u_*(f_s, \mathbf{v}) = \sqrt{\frac{\tau(f_s, \mathbf{v})}{\rho_l}},$$

is the shear velocity, and where ν_l is the kinematic viscosity of the fluid. The use of a constant shear is proved to be sufficient in most applications.

3 | TIME DISCRETIZATION

Let $0 = t^0 < t^1 < t^2 < \cdots < t^N = T$ be a subdivision of the time interval $[0, T]$ and $\Delta t^n = t^{n+1} - t^n$, $n = 0, 1, 2, \ldots, N-1$ be the time steps. Let $\varphi^n, \mathbf{v}^\mathbf{n}, p^n, f_s^n$ be approximations of $\varphi, \mathbf{v}, p, f_s$ respectively available at time t^n. Let $\Omega^n = \{\mathbf{x} \in \Lambda : \varphi^n(\mathbf{x}) = 1\}$ be the approximate liquid region at time t^n. The approximations φ^{n+1}, $\mathbf{v}^{\mathbf{n+1}}$, p^{n+1}, f_s^{n+1} at time t^{n+1} are computed by means of the splitting algorithm illustrated in Figure 2.

3.1 | Modified Stokes step

Given φ^n, $\Omega^n = \{\mathbf{x} \in \Lambda : \varphi^n(\mathbf{x}) = 1\}$, $\mathbf{v}^n$, p^n, f_s^n in Ω^n, we define $\rho_m^n = \rho_m(f_s^n)$, $\mu_m^n = \mu_m(f_s^n)$ and $\alpha_m^n = \alpha_m(f_s^n)$ the density, viscosity, and reaction coefficient, respectively. We are looking for $\mathbf{v}$ and p in $\Omega^n \times [t^n, t^{n+1}]$ such that:

$$\rho_m^n \frac{\partial \mathbf{v}}{\partial t} - 2\nabla \cdot \left(\mu_m^n \mathbf{D}(\mathbf{v})\right) + \alpha_m^n \mathbf{v} + \nabla p = \rho_m^n \mathbf{g}, \tag{10}$$

$$\nabla \cdot \mathbf{v} = 0. \tag{11}$$

Using an implicit Euler scheme, we thus compute $\mathbf{v}^{n+1/2}$, p^{n+1} in Ω^n satisfying:

$$\rho_m^n \frac{\mathbf{v}^{n+1/2} - \mathbf{v}^n}{\Delta t^n} - 2\nabla \cdot \left(\mu_m^n \mathbf{D}(\mathbf{v}^{n+1/2})\right) + \alpha_m^n \mathbf{v}^{n+1/2} + \nabla p^{n+1} = \rho_m^n \mathbf{g}, \tag{12}$$

$$\nabla \cdot \mathbf{v}^{n+1/2} = 0. \tag{13}$$

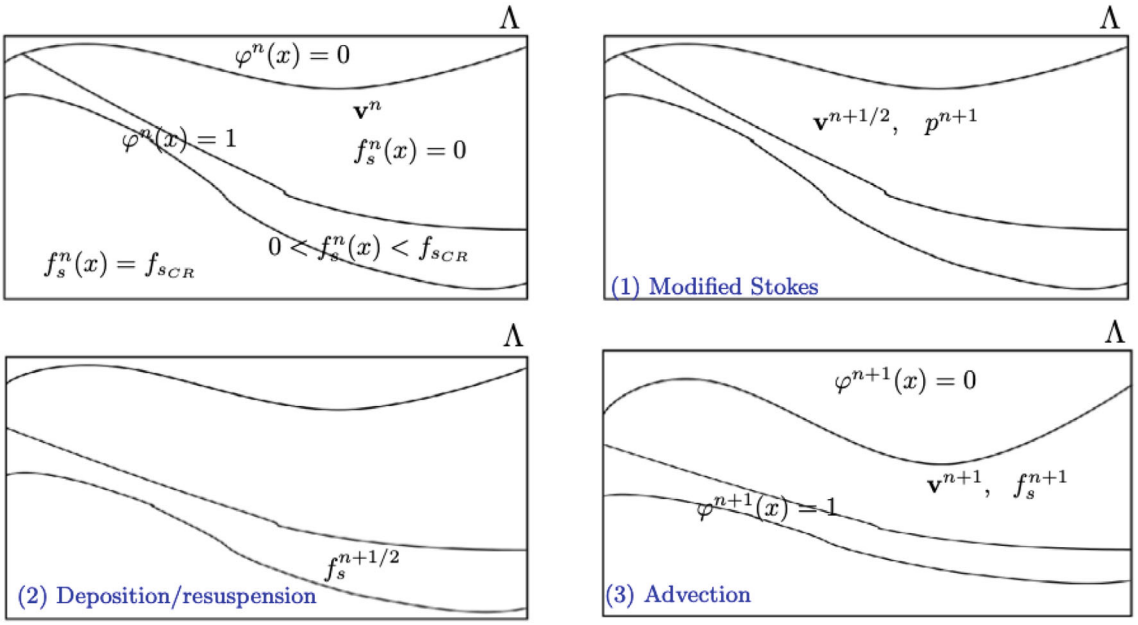

FIGURE 2 Operator splitting algorithm (from t^n to t^{n+1}—left to right, top to bottom). Given φ^n, the liquid domain is $\Omega^n = \{\mathbf{x} \in \Lambda : \varphi^n(\mathbf{x}) = 1\}$, $\mathbf{v}^n$, p^n, f_s^n are known in Ω^n. A modified Stokes problem is solved to obtain the predicted velocity $\mathbf{v}^{n+1/2}$ and the pressure p^{n+1} in Ω^n. Second, the sediment deposition and resuspension problems are solved to obtain a predicted concentration $f_s^{n+1/2}$ in Ω^n. Finally, advection problems are solved to determine the new approximation of the characteristic function φ^{n+1} (and thus the new liquid domain Ω^{n+1}), the corrected velocity $\mathbf{v}^{n+1}$ and solid fraction f_s^{n+1} in Ω^{n+1}. [Colour figure can be viewed at wileyonlinelibrary.com]

3.2 | Sedimentation step

Given f_s^n and $\mathbf{v}^{n+1/2}$ in Ω^n, we are looking for f_s in $\Omega^n \times [t^n, t^{n+1}]$ such that:

$$\frac{\partial f_s}{\partial t} + \nabla \cdot \left(F_l(f_s) \left(k v_{stokes} \frac{\mathbf{g}}{\|\mathbf{g}\|} - A(f_s, \mathbf{v}^{n+1/2}) \nabla f_s \right) \right) = 0. \tag{14}$$

A splitting method involving a finite-volume method for conservation laws (see for instance Reference 31), and a finite differences method is used to solve (14) and decouple it into the deposition and resuspension operators. It consists in solving successively in $\Omega^n \times [t^n, t^{n+1}]$:

$$\frac{\partial f_s}{\partial t} + \nabla \cdot \left(F_l(f_s) k v_{Stokes} \frac{\mathbf{g}}{\|\mathbf{g}\|} \right) = 0, \tag{15}$$

$$\frac{\partial f_s}{\partial t} - \nabla \cdot \left(F_l(f_s) A(f_s, \mathbf{v}^{n+1/2}) \nabla f_s \right) = 0. \tag{16}$$

We denote by $f_s^{n+1/2}$ the solution obtained at t^{n+1} in Ω^n.

3.3 | Advection step

Given φ^n, $f_s^{n+1/2}$, and $\mathbf{v}^{n+1/2}$ in Ω^n, we are looking for φ, $\mathbf{v}$, and f_s such that:

$$\frac{\partial \varphi}{\partial t} + \mathbf{v} \cdot \nabla \varphi = 0, \tag{17}$$

$$\frac{\partial f_s}{\partial t} + \mathbf{v} \cdot \nabla f_s = 0, \tag{18}$$

$$\frac{\partial \mathbf{v}}{\partial t} + (\mathbf{v} \cdot \nabla)\mathbf{v} = 0, \tag{19}$$

between time t^n and t^{n+1}. These equations are solved with the characteristics method.[46,47] We denote $\varphi^{n+1}, f_s^{n+1}, \mathbf{v}^{n+1}$, the solutions obtained at t^{n+1}, which are respectively defined by:

$$\varphi^{n+1}(\mathbf{x} + \Delta t^n \mathbf{v}^{n+1/2}(\mathbf{x})) = \varphi^n(\mathbf{x}), \tag{20}$$

$$f_s^{n+1}(\mathbf{x} + \Delta t^n \mathbf{v}^{n+1/2}(\mathbf{x})) = f_s^{n+1/2}(\mathbf{x}), \tag{21}$$

$$\mathbf{v}^{n+1}(\mathbf{x} + \Delta t^n \mathbf{v}^{n+1/2}(\mathbf{x})) = \mathbf{v}^{n+1/2}(\mathbf{x}), \tag{22}$$

for all $\mathbf{x} \in \Omega^n$. The new liquid domain is then defined as $\Omega^{n+1} = \{\mathbf{x} \in \Lambda; \varphi^{n+1}(\mathbf{x}) = 1\}$.

4 | SPACE DISCRETIZATION

The splitting algorithm allows to decouple the diffusion, advection, and deposition/resuspension phenomena. In order to take advantage of this situation, two grids are used for space discretization following References 26,29,48,49. They are illustrated in Figure 3 (in two space dimensions): a regular grid of small structured cells (left) is used to solve the deposition/resuspension problems (15), (16), and the advection problems (20)–(22), while an unstructured tetrahedral finite element mesh (right) is used to solve the diffusion problem (13). The structured grid is chosen to be finer than the finite element grid, in order to avoid numerical diffusion when implementing (20) (remember that φ is discontinuous across the liquid–air interface), while keeping reasonable the computational cost of solving the modified Stokes problem.

On the one hand, let $\mathcal{T}_H$ be a finite element tetrahedral discretization of $\overline{\Lambda}$, with typical size H. On the other hand, the cavity Λ is embedded into a parallelepipedic box discretized into a structured Cartesian grid C_h, which is made out of

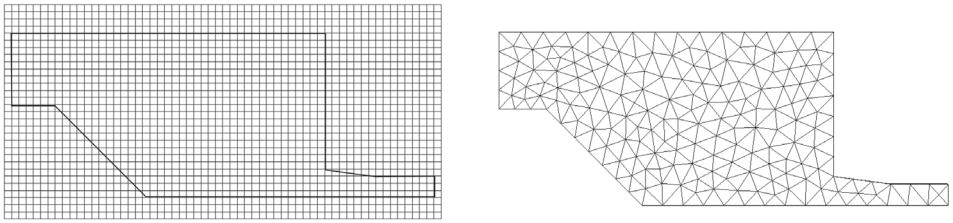

FIGURE 3 Two-grid method (2D sketch): The advection and the deposition/resuspension problems are solved on a structured grid of small rectangular cells (left), and the diffusion problem is solved on a coarser unstructured finite element mesh (right).

small cells whose dimensions are denoted by $(\Delta x, \Delta y, \Delta z)$, with a typical size $h := \max\{\Delta x, \Delta y, \Delta z\}$. We label each cell by the indices (ijk), and denote by C_{ijk} a generic cell of $\mathcal{C}_h$. Following Reference 29, we typically advocate $H \simeq 3h - 5h$ in the numerical experiments presented below.

4.1 | Modified Stokes step

Continuous piecewise linear finite element approximations of $\mathbf{v}^{n+1/2}$ and p^{n+1} are obtained as in Reference 25. More precisely, let us define $V^n = H^1(\Omega^n)$ and $Q^n = L^2(\Omega^n)$. The variational formulation corresponding to the Stokes problem (13) consists in finding the velocity $\mathbf{v}^{n+1/2} \in (V^n)^3$ and the pressure $p^{n+1} \in Q^n$, satisfying the essential boundary conditions on $\partial\Omega^n$, and such that:

$$\int_{\Omega^n} \left(\rho_m^n \frac{\mathbf{v}^{n+1/2} - \mathbf{v}^n}{\Delta t^n} \cdot \mathbf{w} + 2\mu_m^n \mathbf{D}(\mathbf{v}^{n+1/2}) : \mathbf{D}(\mathbf{w}) + \alpha_m^n \mathbf{v}^{n+1/2} \cdot \mathbf{w} \right) d\mathbf{x} - \int_{\Omega^n} p^{n+1} \nabla \cdot \mathbf{w} d\mathbf{x} - \int_{\Omega^n} q \nabla \cdot \mathbf{v}^{n+1/2} d\mathbf{x} = \int_{\Omega^n} \rho_m^n \mathbf{g} \cdot \mathbf{w} d\mathbf{x}, \tag{23}$$

for all $\mathbf{w}$ and q the velocity and pressure test functions, compatible with the essential boundary conditions on $\partial\Omega^n$. Finite element approximations of $\mathbf{v}^{n+1/2}$ and p^{n+1} are implemented on $\mathcal{T}_H$, obtained using $\mathbb{P}_1^B/\mathbb{P}_1$ finite elements, where $\mathbb{P}_1^B$ is the classical space of polynomials of first degree on K enriched with a bubble function.[50]

Let φ_H^n be the volume fraction of liquid defined by the continuous piecewise linear finite element approximation of φ^n defined by its values at the vertices of T_H. The liquid region Ω_H^n is defined by the union of all tetrahedra of the finite element mesh T_H having (at least) one of its vertices P with a value $\varphi_P^n > 0.5$. The finite element spaces are defined as follows:

$$V_H^n = \left\{ v_H \in C^0(\overline{\Omega_H^n}) : \quad v_H|_K \in \mathbb{P}_1^B, \quad \forall K \in T_H, K \subset \overline{\Omega_H^n} \right\},$$

$$Q_H^n = \left\{ q_H \in C^0(\overline{\Omega_H^n}) : \quad q_H|_K \in \mathbb{P}_1, \quad \forall K \in T_H, K \subset \overline{\Omega_H^n} \right\}.$$

Let us define $\rho_{m,H}^n$, $\mu_{m,H}^n$, and $\alpha_{m,H}^n$ as the piecewise constant approximations of ρ_m^n, μ_m^n, and α_m^n on each tetrahedron, respectively. The finite element approximation of (23) consists in finding the velocity $\mathbf{v}_H^{n+1/2} \in (V_H^n)^3$ and the pressure $p_H^{n+1} \in Q_H^n$, satisfying the essential boundary conditions on $\partial\Omega_H^n$, and such that:

$$\int_{\Omega_H^n} \left(\rho_{m,H}^n \frac{\mathbf{v}_H^{n+1/2} - \mathbf{v}_H^n}{\Delta t^n} \cdot \mathbf{w} + 2\mu_{m,H}^n \mathbf{D}\left(\mathbf{v}_H^{n+1/2}\right) : \mathbf{D}(\mathbf{w}) + \alpha_{m,H}^n \mathbf{v}_H^{n+1/2} \cdot \mathbf{w} \right) d\mathbf{x} - \int_{\Omega_H^n} p_H^n \nabla \cdot \mathbf{w} d\mathbf{x} - \int_{\Omega_H^n} q \nabla \cdot \mathbf{v}_H^{n+1/2} d\mathbf{x} = \int_{\Omega_H^n} \rho_{m,H}^n \mathbf{g} \cdot \mathbf{w} d\mathbf{x},$$

for all $\mathbf{w} \in (V_H^n)^3$ and $q \in Q_H^n$ the velocity and pressure test functions, compatible with the essential boundary conditions on $\partial\Omega_H^n$. The corresponding linear system is solved with a preconditioned GMRES method. The finite element approximation $\mathbf{v}_H^{n+1/2}$ is then interpolated onto the grid $\mathcal{C}_h$.[51]

4.2 | Sedimentation step

From now on, and for all numerical experiments presented in Section 5, the gravity $\mathbf{g}$ is assumed to be aligned with the $\vec{Oz}$ axis. We assume that $(f_s)_{ijk}^n$ and $(\mathbf{v})_{ijk}^{n+1/2}$ are known in each cell ijk of $\mathcal{C}_h$. Following Reference 25, (15) is solved to obtain $f_s^{n+1/4}$ with a finite volumes scheme:

$$(f_s)_{ijk}^{n+\frac{1}{4}} = (f_s)_{ijk}^n - \frac{\Delta t^n}{\Delta z}\left((FV_Z)_{ijk+\frac{1}{2}}^n - (FV_Z)_{ijk-\frac{1}{2}}^n\right), \tag{24}$$

where $(FV_Z)^n$ are fluxes defined by the Godunov method.[31] Then, the piecewise constant approximation $\tau_{ijk}^{n+1/4}$ of the tangential stress defined by (9) is computed in cell ijk at time t^n:

$$\tau_{ijk}^{n+1/4} = 2\mu_m((f_s)_{ijk}^{n+1/4})\|\mathbf{D}_{ijk}^{n+1/2}\mathbf{n}_{ijk}^{n+1/4} - \left(\mathbf{D}_{ijk}^{n+1/2}\mathbf{n}_{ijk}^{n+1/4}\cdot\mathbf{n}_{ijk}^{n+1/4}\right)\mathbf{n}_{ijk}^{n+1/4}\|, \tag{25}$$

where $\mathbf{D}_{ijk}^{n+1/2} = \mathbf{D}\left(\mathbf{v}_{ijk}^{n+1/2}\right)$ and $\mathbf{n}_{ijk}^{n+1/4}$ are computed using centered finite differences. Then we compute $A_{ijk}^{n+\frac{1}{4}} = K_r\left(\frac{\tau_{ijk}^{n+\frac{1}{4}}-\tau_{CR}}{\tau_{CR}}\right)_+$. Problem (16) is then solved to obtain $f_s^{n+1/2}$ on the structured grid $\mathcal{C}_h$ using an explicit finite differences scheme:

$$\frac{(f_s)_{ijk}^{n+\frac{1}{2}} - (f_s)_{ijk}^{n+\frac{1}{4}}}{\Delta t^n} = (FD_X)_{ijk}^{n+\frac{1}{4}} + (FD_Y)_{ijk}^{n+\frac{1}{4}} + (FD_Z)_{ijk}^{n+\frac{1}{4}}. \tag{26}$$

The diffusion terms are given by, for example, $(FD_X)_{ijk}^{n+\frac{1}{4}} = \frac{A_{i+\frac{1}{2}jk}^{n+\frac{1}{4}}F_{i+\frac{1}{2}jk}^{n+\frac{1}{4}} - A_{i-\frac{1}{2}jk}^{n+\frac{1}{4}}F_{i-\frac{1}{2}jk}^{n+\frac{1}{4}}}{\Delta x^2}$. Similar definitions hold for $(FD_Y)_{ijk}^{n+\frac{1}{4}}$ and $(FD_Z)_{ijk}^{n+\frac{1}{4}}$. Here, for example,

$$F_{i+\frac{1}{2}jk}^{n+\frac{1}{4}} = F_l\left(\frac{(f_s)_{i+1jk}^{n+\frac{1}{4}} + (f_s)_{ijk}^{n+\frac{1}{4}}}{2}\right)\left((f_s)_{i+1jk}^{n+\frac{1}{4}} - (f_s)_{ijk}^{n+\frac{1}{4}}\right),$$

Similar definitions hold for $F_{ij+\frac{1}{2}k}^{n+\frac{1}{4}}$, $F_{ijk+\frac{1}{2}}^{n+\frac{1}{4}}$, $F_{i+\frac{1}{2}jk}^{n+\frac{1}{4}}$, $F_{ij-\frac{1}{2}k}^{n+\frac{1}{4}}$, and $F_{ijk-\frac{1}{2}}^{n+\frac{1}{4}}$. The stability of this explicit scheme is subject to the following condition (where $h = \min(\Delta x, \Delta y, \Delta z)$):[52]

$$\left|\frac{\Delta t^n \max_{i,j,k}\left(A_{ijk}^{n+\frac{1}{4}}\right)}{h^2}\right| \leq \frac{1}{6}. \tag{27}$$

4.3 | Advection step

Equations (20)–(22) are solved on the structured grid $\mathcal{C}_h$ with an, unconditionally stable, forward characteristics method, using piecewise constant approximations of each field on $\mathcal{C}_h$. The advection of a cell C_{ijk} consists in transporting the quantities φ_{ijk}^n, $f_{s_{ijk}}^{n+1/2}$, and $\mathbf{v}_{ijk}^{n+1/2}$ along the linearized characteristics $\Delta t^n\mathbf{v}_{ijk}^{n+1/2}$, with a conservative redistribution of the transported quantities onto the grid.[29] Figure 4 (left) shows, in two dimensions of space, how the forward characteristics method with redistribution of the quantities onto the grid advects a single cell.

The algorithm includes a variation of the heuristic SLIC algorithm,[30] in order to reduce the numerical diffusion when transporting the variable φ_{ijk}^n, which is a step function. Figure 4 (right) shows how the forward characteristics method

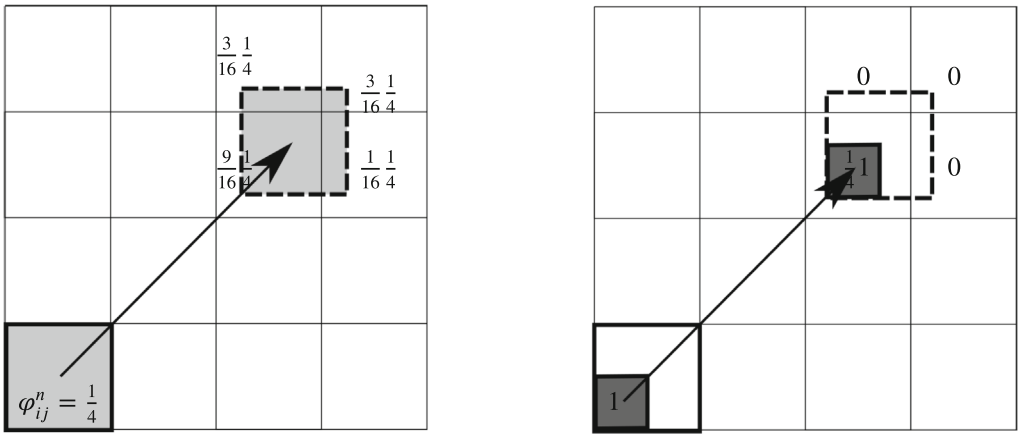

FIGURE 4 An example of two dimensional advection and projection when the volume fraction of liquid in the cell is $\varphi_{ij}^n = \frac{1}{4}$. Left: without SLIC, the volume fraction of liquid is advected and projected on four cells, with contributions (from the top left cell to the bottom right cell) $\frac{3}{16}\frac{1}{4}$, $\frac{1}{16}\frac{1}{4}$, $\frac{9}{16}\frac{1}{4}$, $\frac{3}{16}\frac{1}{4}$. Right: with SLIC, the volume fraction of liquid is first pushed at one corner, then it is advected and projected on one cell only, with contribution $\frac{1}{4}$ in one cell instead of four.

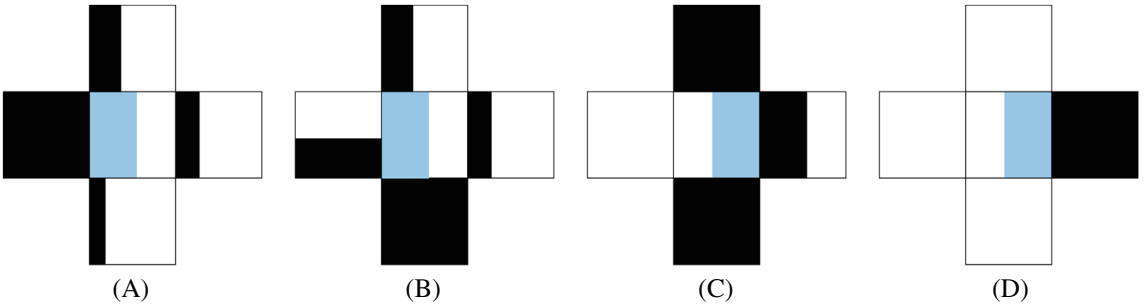

FIGURE 5 Effect of the two dimensional SLIC algorithm on the cell center for four possible interfaces. The quantity φ_{ij}^n, in blue, is pushed back to the sides of C_{ij} depending on the values of φ^n in the neighboring cells, in black. The cases (A) through (D) correspond to four examples of configurations of the neighboring cells. [Colour figure can be viewed at wileyonlinelibrary.com]

is adapted by rearranging the quantities within a cell before advection. Figure 5 shows, on a simple 2D sketch, how to rearrange those quantities depending on the neighboring values of the field.

Additional post-processing techniques are implemented in order to avoid two effects: (i) the loss of liquid/sediment mass that has been advected outside the computational domain and (ii) the numerical compression of the variables φ_{ijk}^n, $f_{s_{ijk}}^{n+1/2}$ after transport. First, we redistribute the quantities in the cells that have been advected outside the domain. For each cell outside the domain, we identify the partially empty cells in its neighborhood using a distance function, and re-distribute the excess recursively starting from closest to the initial cell. Cells are typically advected outside the domain when the CFL number is large or when the domain has curved boundaries. Second, we "decompress" the cells inside the domain for which $\varphi_{ijk}^n > 1$ and/or $(f_s)_{ijk}^{n+1/2} > fs_{CR}$. This is achieved also by redistributing the excess quantities to other cells. The decompression of the excess of φ_{ijk}^n is achieved as in Reference 29 in a global manner. For the decompression of $(f_s)_{ijk}^{n+1/2}$, we identify again the partially empty cells in the neighborhood of the overfilled cell using a distance function, and we redistribute the excess sediment randomly to cells where $(f_s)_{ijk}^{n+1/2} < fs_{CR}$. The random choice prevents the algorithm to introduce a privileged direction for the redistribution and acts as a random local diffusion effect.

The approximations φ_{ijk}^{n+1}, $(f_s)_{ijk}^{n+1}$, and $\mathbf{v}_{ijk}^{n+1}$ are then interpolated back onto the coarse finite element mesh $\mathcal{T}_H$,[51] and the new liquid region Ω_H^{n+1} is defined as the union of all liquid finite elements of $\mathcal{T}_H$ (elements with at least one vertex P such that $\varphi_P^{n+1} > 0.5$). Physical quantities ρ_m^{n+1}, μ_m^{n+1}, and α_m^{n+1} are computed following (4), (5), and (6), on the structured grid C_h, based on the piecewise constant approximations of f_s^{n+1}, and then interpolated on the finite element mesh as well.

Under the CFL condition, and provided that $H \simeq 3h - 5h$, the overall convergence rate of the numerical method is one. Thus, when dividing H, h, and Δt by two, the error should be divided by two.

5 | NUMERICAL EXPERIMENTS

Numerical experiments allow us to validate the accuracy and efficiency of our mathematical model and numerical method. All simulations have been performed on a system equipped with Intel®Xeon(R) CPU E5-1650 v3 @ 3.50 GHz × 12 and 64 GB RAM.

5.1 | Sediment flushing

We consider first a flushing experiment.[53] This experiment has been discussed in previous works,[25] where the absence of resuspension effects in the physical model had proved to be cumbersome. A bed load of non-cohesive sediments, initially at rest at the bottom of a channel, as illustrated in Figure 6. It is performed in a laboratory flume of width 0.2 (m). The bed load of non-cohesive sediment is composed by sand ($d_* = 7.6 \cdot 10^{-4}$ (m), $\rho_s = 2650$ (kg m^{-3}), $\rho_l = 1750$ (kg m^{-3})). Under vertical gravity forces, the liquid flows out of the domain via the valve on the right, and the sediment is flushed by the flow. An outflow condition is enforced by imposing a discharge of $q_0 = 0.0079$ (m^3/s) on the bottom right part of the domain (which corresponds to an outflow velocity of approx. 0.132 m/s). A free surface lies at the top of the domain. Slip boundary conditions are imposed everywhere else. Initially the liquid and sediments are at rest.

The experiment is run with $T = 3$ (s), and three discretizations are considered (a coarse mesh with 6684 elements, 2446 nodes, 51,480 cells, $H \simeq 0.045$ (m), $h \simeq 0.01$ (m) and $\Delta t = 0.006$, an intermediate mesh with 26,079 elements, 9124 nodes, 205,920 cells, $H \simeq 0.025$ (m), $h \simeq 0.005$ (m) and $\Delta t = 0.003$, and a fine mesh with 45,600 elements, 15,772 nodes, 369,600 cells, $H \simeq 0.02$ (m), $h \simeq 0.003$ (m) and $\Delta t = 0.0022$). Figure 7 shows the convergence of sediments profiles at time $T = 3$ (s) for the various discretizations.

From now on, we consider the intermediate mesh to perform a sensitivity analysis with respect to the parameters. Let us set $\varepsilon = 10^{-11}$, $f_{s_{CO}} = 0.4699$, $\tau_{CR} = 0.05$ (N/m^2) and consider several strictly positive values for the parameter K_r. Figure 8 displays the snapshots of the shear stress on the structured grid for various times t, and shows that the shear stress is appropriately located at the interface.

Figure 9 shows the sediment bedload at $t = 40$ (s), for $\tau_{CR} = 0.05$ (N/m^2) and various values of K_r. We observe that, with $K_r = 10^{-3}$, we do not have enough resuspension effects, while the results with $K_r = 10^{-2}$ and $K_r = 10^{-1}$ are very similar

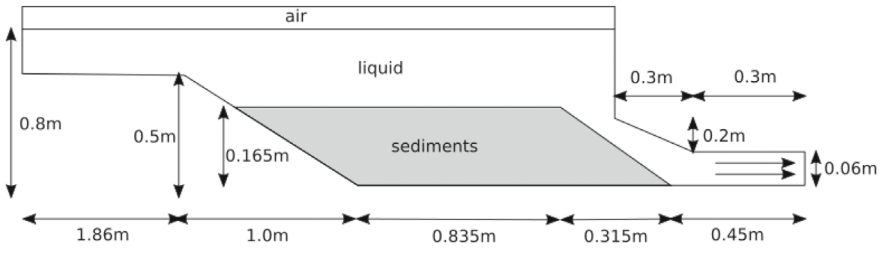

FIGURE 6 Sediments flushing. Sketch of the geometrical domain and numerical setup (similar as in Reference 53).

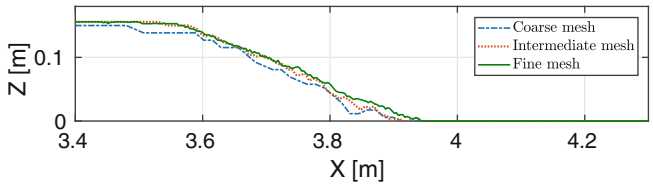

FIGURE 7 Sediment flushing. Mesh convergence at $t = 3$ (s) with resuspension ($K_r = 10^{-2}$, $\tau_{CR} = 0.05$ (N/m^2), $\varepsilon = 10^{-11}$, $f_{s_{CO}} = 0.4699$) [Colour figure can be viewed at wileyonlinelibrary.com]

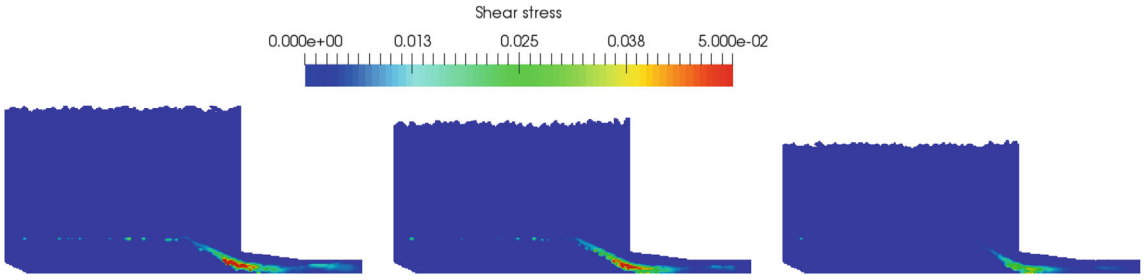

FIGURE 8 Sediment flushing. Snapshots of the shear stress at $t = 2.5, 10$ (s) and $t = 20$ (s) (left to right). [Colour figure can be viewed at wileyonlinelibrary.com]

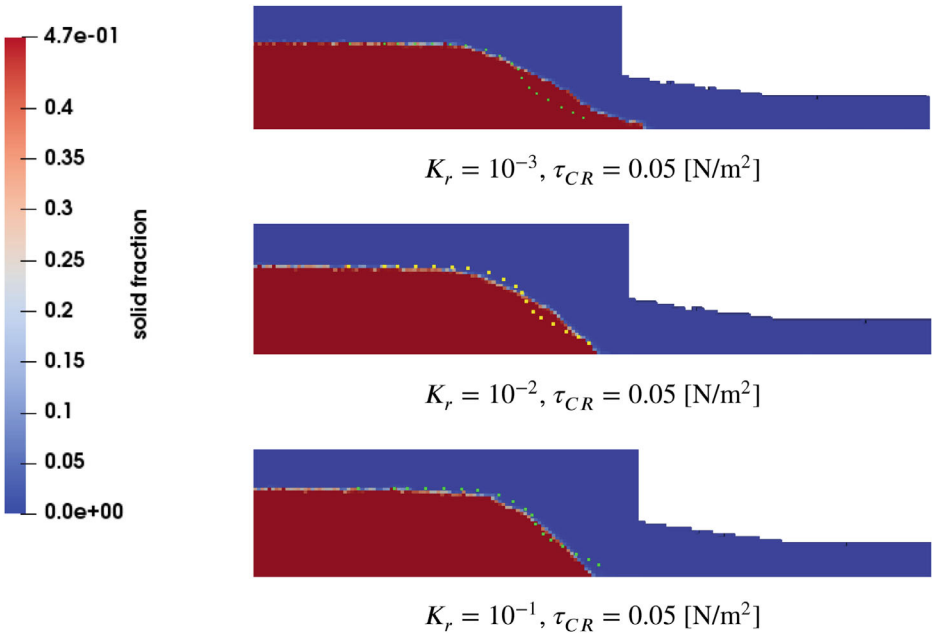

FIGURE 9 Sediment flushing. Sediment profile at $t = 40s$ for $\varepsilon = 10^{-11}$ and various resuspension parameters K_r. Plotted dots represent the experimental results. [Colour figure can be viewed at wileyonlinelibrary.com]

and close to the experimental results. Figure 10 illustrates snapshots of the sediment bedload and of the experimental results (dotted points) over time for $K_r = 10^{-2}$, $\tau_{CR} = 0.05$ (N/m^2) and at several times. It shows that the introduction of resuspension effects is necessary to appropriately match experimental results.

Finally, we conduct a convergence error analysis for the bedload profile towards the experimental results at $T = 42$ (s), $K_r = 10^{-2}$ and $\tau_{CR} = 0.05$ (N/m^2). Figure 11 illustrates the convergence order of the error between experimental and computed sediment bedload profile, in the discrete L^2-norm for the given meshes. The convergence order is, as expected, approx. equal to one. Table 1 summarizes the average CPU time (in (s)) per time step of the operator splitting algorithm. Because of the stability condition (27), the resuspension step is solved with smaller time substeps at each time step of the diffusion operator. For this numerical experiment, 5 substeps are performed per time step. One can observe that the Stokes problem remains the expensive step, but, depending of the number of substeps, the resuspension step is computationally not negligible.

5.2 | Wall-jet scouring experiment

Let us consider the scouring experiment described in Reference 54 and illustrated in Figure 12. It is performed in a glass-walled horizontal flume of width 0.74 (m) and depth 0.2 (m). A rigid plate is installed in the flume to create a

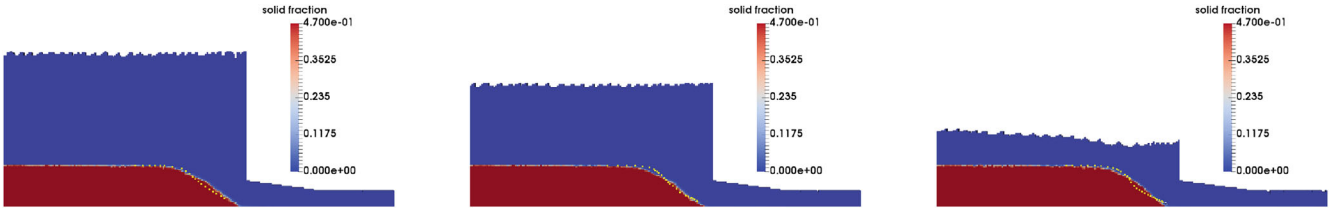

FIGURE 10 Sediment flushing. Snapshots of the sediment profile at $t = 20, 30$ (s) and $t = 40$ (s) (left to right) for $K_r = 10^{-2}$, $\tau_{CR} = 0.05$ (N/m^2). Plotted dots represent experimental data. [Colour figure can be viewed at wileyonlinelibrary.com]

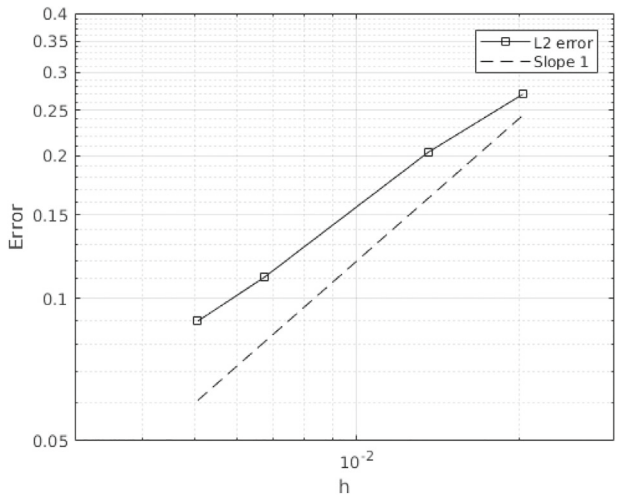

FIGURE 11 Sediment flushing. L^2 convergence error on the sediment profile at $t = 10$ (s).

TABLE 1 Sediment flushing

		Sedimentation step		Advection step	
	Stokes step	Deposition	Resuspension	Advection	Decomp/SLIC
Coarse	0.38	0.06	0.42	0.17	0.11
Intermediate	5.2	0.94	6.32	2.66	1.57
Fine	25.8	4.65	31.2	13.2	7.85

Note: Average CPU time per time step in (s) for each operator, for the coarse, intermediate and fine meshes ($\epsilon = 10^{-11}$, $K_r = 10^{-2}$, $\tau_{CR} = 0.05$ (N/m^2), 5 substeps per time step). Total computational time of 42 (s).

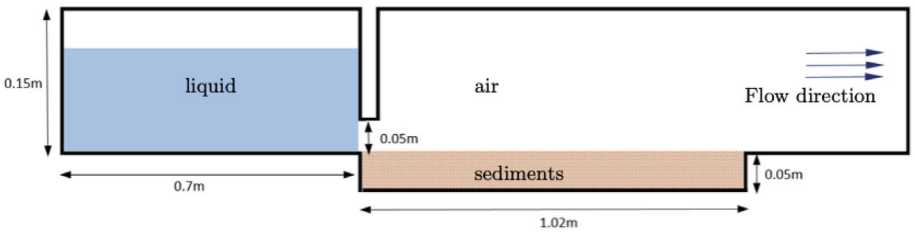

FIGURE 12 Wall-jet scouring. Sketch of the geometrical domain and numerical setup (similar as in Reference 54). [Colour figure can be viewed at wileyonlinelibrary.com]

reservoir on the left, with a gate of height 0.05 (m). The water height in the reservoir is equal to 0.15 (m). A layer of non-cohesive sand particles of diameter $d_* = 0.85 \cdot 10^{-3}$ (m) is laid on the right side of the setup, with $\rho_s = 2650$ (kg m^{-3}), and $\rho_l = 1750$ (kg m^{-3}). At $t = 0$, the gate is opened. Free outflow conditions are applied on the right part of the domain, while slip and no-slip boundary conditions are applied on the lateral and top surfaces, and on the surfaces in contact with sediment, respectively. After about $T = 3.5$ (s), the evolution of the scour hole and ridge become stationary.

We compare the experimental results and the numerical results by comparing the sand profiles and the water levels as well as the evolution of the scour hole diameter. We first evaluate the convergence of the numerical method when considering $\epsilon = 10^{-11}$, $f_{s_{CO}} = 0.4699$, $K_r = 10^{-3}$, and $\tau_{CR} = 0.05$ (N/m^2), and three discretizations (coarse: 6750 elements, 2442 nodes, 19,500 cells, $H \simeq 0.037$, $h \simeq 0.0043$ and $\Delta t = 0.05$, intermediate: 25,956 elements, 9028 nodes, 81,900 cells, $H \simeq 0.02$, $h \simeq 0.0025$ and $\Delta t = 0.025$, and fine: 102,888 elements, 35,040 nodes, 319,800 cells, $H \simeq 0.011$, $h \simeq 0.0014$, and $\Delta t = 0.0125$). Figure 13 illustrates the sediment and the water profiles for all three meshes. Note that resuspension effects are instrumental for the scouring to occur.

We consider the set of parameters: $K_r = 10^{-3}$, $f_{s_{CO}} = 0.6099$, $\epsilon = 10^{-11}$, with $\tau_{CR} = 0.05$ (N/m^2). Figure 14 (left column) illustrates the results for the constant critical shear model at $t = 1.5$ (s) and $t = 3.5$ (s). We observe that, the numerical

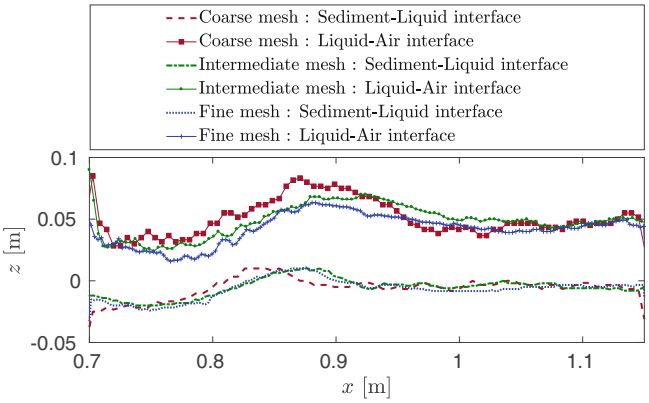

FIGURE 13 Wall-jet scouring. Convergence of the numerical solution when discretization parameters go to zero: Sediment and water profiles at $t = 1$ (s) for various mesh sizes. [Colour figure can be viewed at wileyonlinelibrary.com]

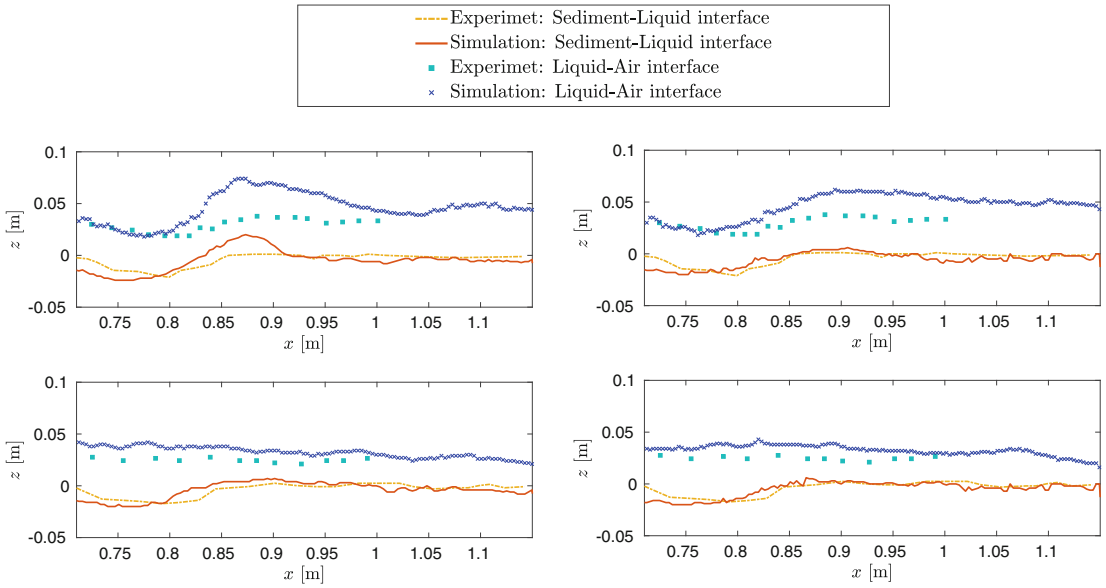

FIGURE 14 Wall-jet scouring. Sediment and water profiles in comparison with the experimental results. Top: at $t = 1.5$ (s); bottom: at $t = 3.5$ (s). Left: Numerical results with the constant critical shear model. Right: Numerical results with the Shields critical shear model. [Colour figure can be viewed at wileyonlinelibrary.com]

results are comparable with the experimental results[54] in the stationary state (at 3.5 s). However, in the transient phase (at 1.5 s), the numerical solution does not match well the experiments. These results are very similar to those obtained with the Coulomb-Shear model mentioned in Reference 54. Figure14 (right column) shows the sediment and liquid profiles for the numerical results obtained with the Shields critical shear model, inspired by Khanpour and Zarrati,[54] which allows to improve the results during the transient phase.

Figure 15 shows snapshots at various times to illustrate that the scouring process simulations with the Shields model better match the experiments. Figure 16 illustrates the discrepancy between the numerical solutions for several meshes, and the experimental measurements, when using the Shields critical shear model (sediment and water profiles). Figure 17 (left) illustrates the time evolution of the maximal diameter of the scour hole, which is similar for both the experimental

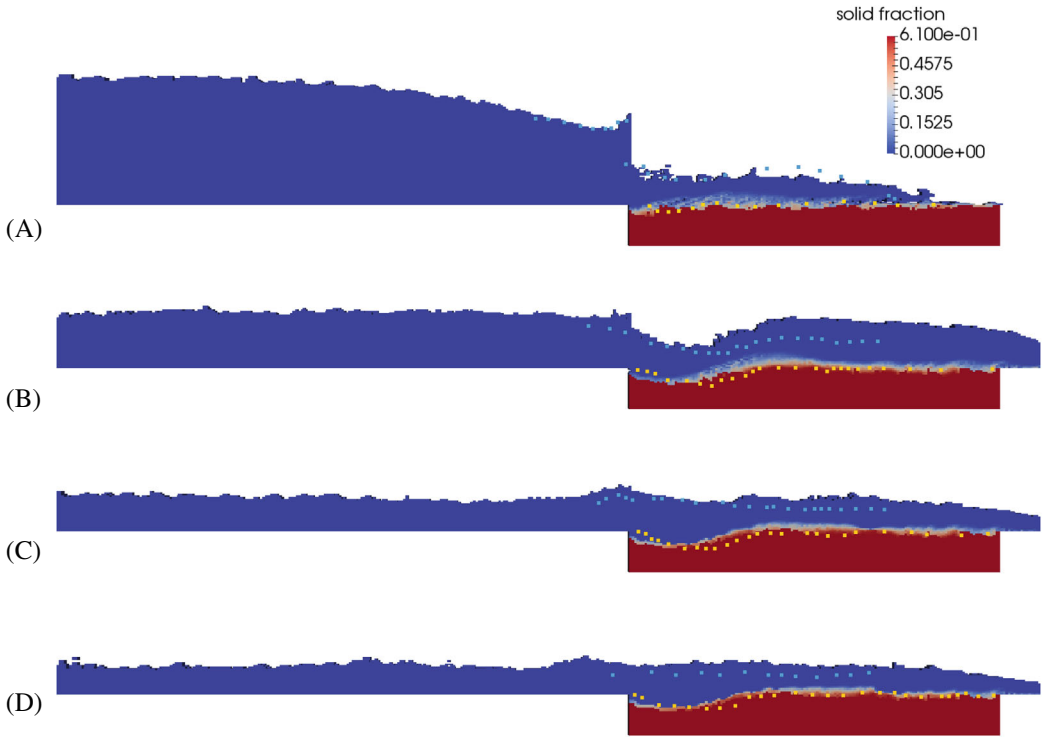

FIGURE 15 Wall-jet scouring. Snapshots of sediment profiles at (A) $t = 0.3$ (s) (B) $t = 1.5$ (s) (C) $t = 2.7$ (s), and (D) $t = 3.5$ (s) with the Shields critical shear for $K_r = 10^{-3}$, $f_{s_{CO}} = 0.6099$, and $\varepsilon = 10^{-11}$. The yellow (resp. the light blue) dots represent the experimental sediment level (resp. liquid level). [Colour figure can be viewed at wileyonlinelibrary.com]

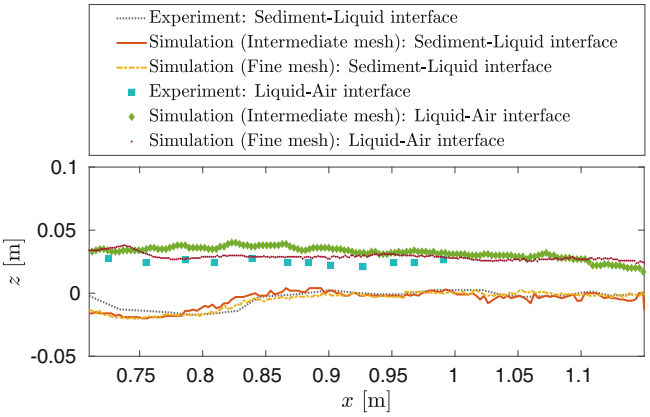

FIGURE 16 Plot of sediment and water levels on the intermediate and the fine meshes [Colour figure can be viewed at wileyonlinelibrary.com]

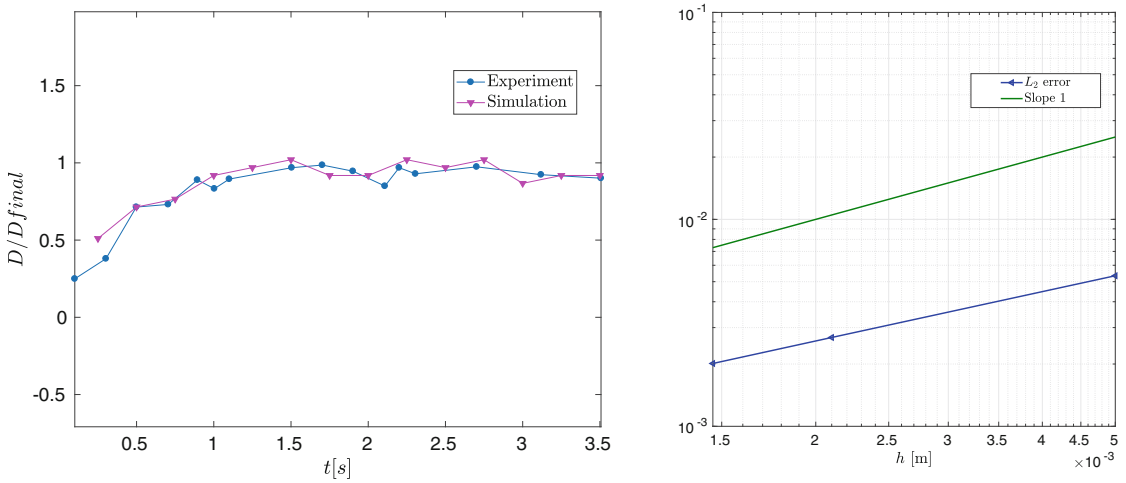

FIGURE 17 Wall-jet scouring. Left: scour-hole width over time: Numerical results with the Shields critical shear in comparison with the experimental results. Right: L^2 error between the experiment and the numerical sediment heights for various meshes at $t = 3.5$ (s). [Colour figure can be viewed at wileyonlinelibrary.com]

TABLE 2 Wall-jet scouring

		Sedimentation step		Advection step	
	Stokes step	**Deposition**	**Resuspension**	**Advection**	**Decomp/SLIC**
Coarse	0.34	0.021	2.76	0.14	0.13
Intermediate	5.24	0.32	43.8	2.18	1.98
Fine	83.1	5.1	700.2	34.5	32.5

Note: Average CPU time per time step in (s) for each operator, for the coarse mesh ($\Delta t = 0.05$ s), intermediate mesh ($\Delta t = 0.025$ s), and fine mesh ($\Delta t = 0.0125$ s) all defined earlier. The results are given for the chosen parameters $\epsilon = 10^{-11}$, $K_r = 10^{-3}$, and $\tau_{CR} = 0.05$ (N/m^2) and over a computation time of 3.5 (s).

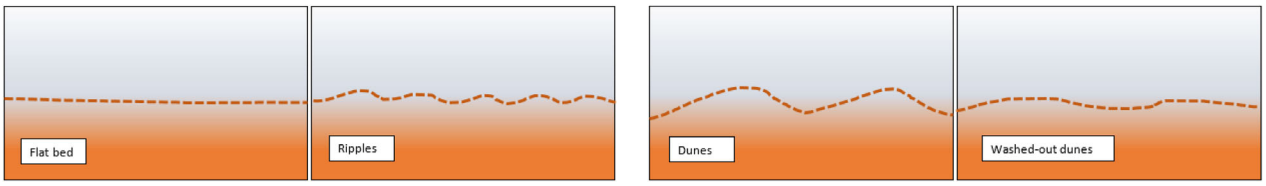

FIGURE 18 An illustration of various bedforms configurations [Colour figure can be viewed at wileyonlinelibrary.com]

and the numerical solutions; the slight overestimation of the liquid level at all times is also observed in Reference 54. Figure 17 (right), and shows the L^2 error on the sediment height, which exhibits a first-order convergence order.

Table 2 illustrates the average CPU time (in (s)) per time step for each operator. In this case, 27 sub-steps are used in average to solve the resuspension operator.

5.3 | River-stream simulation

Finally we would like to reproduce self-generated bedforms (dunes) in sediment bed rivers. Dunes in river mechanics have complex physical ascetics, since the ripples and dunes form only under a relatively limited range of flow condition, in terms of, for example, the domain's typical size, the size of the particles, or the velocity (hence the shear stress and the Reynolds number). There exist various situations for the bedforms.[55] Figure 18 illustrates various configurations typically characterized by their height and wavelength.[56,57]

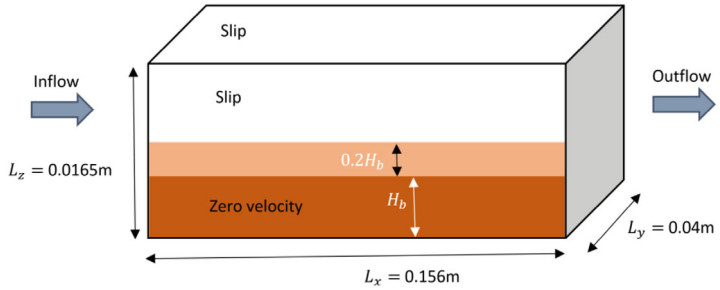

FIGURE 19 River-stream simulation. A layout of the experimental setup: The light brown particles are moving particles; the dark brown particles are fixed. [Colour figure can be viewed at wileyonlinelibrary.com]

TABLE 3 River-stream simulation

	Case 1	Case 2	Case 3	Case 4
Description	Ripple	Large dune	Washing out	Washed out
Reynolds number $Re_b = 2U_bH_b/\nu$	6000	8000	10,000	12,000
Mean velocity U_b (m/s)	0.39	0.52	0.65	0.78

Note: Bedform topologies based on the mean velocity and Reynolds number.

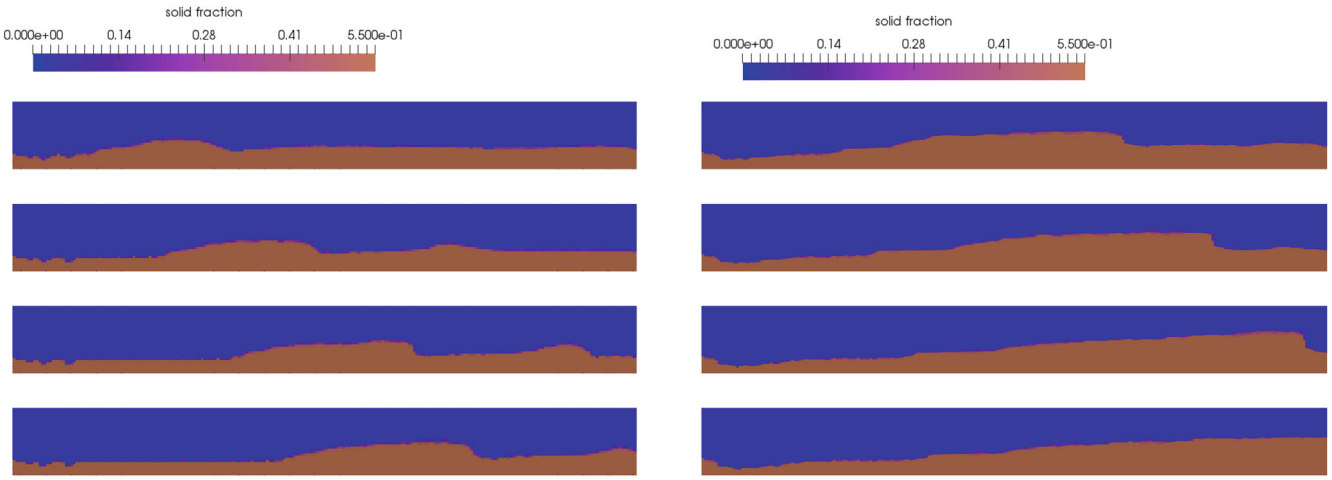

FIGURE 20 River-stream simulation. Left: Case 1 ($U_b = 0.39$ m/s), top to bottom: Snapshots of sediment profiles for $t = 5, 10, 15$ (s) and $t = 20$ (s) ($K_r = 10^{-6}$). Right: Case 2 ($U_b = 0.52$ m/s), top to bottom: snapshots of sediment profiles for $t = 5, 10, 12.5$ (s) and $t = 15$ (s) ($K_r = 10^{-6}$). [Colour figure can be viewed at wileyonlinelibrary.com]

Figure 19 shows the numerical setup. A fixed sediment layer of height $H_b = 0.005$ (m) is placed at the bottom of the domain, covered by a layer of free sediments. The characteristics of the sediment particles are $d_* = 0.5 \cdot 10^{-3}$ (m), $\rho_s = 2500$ (kg m^{-3}). The liquid density is $\rho_l = 1000$ (kg m^{-3}) and the liquid viscosity is $\mu_l = 1.5 \cdot 10^{-3}$ (N s m^{-2}). An inflow condition is enforced on the left side of the domain and free outflow conditions are imposed on the right side. Slip boundary conditions are enforced on all lateral walls above the fixed sediment height. Four physical setups occur in experimental studies,[55-57] and are summarized in Table 3. The focus here is on simulating the ripples and large dunes regimes.

We consider an inflow velocity $\mathbf{u}_{in} = (u_x(z), 0, 0)^T \mathbb{I}_{z>H_b}$, with a logarithmic profile:

$$u_x(z) = \frac{Q\,(1 + 2.5 \ln(1+z))}{L_y\,(2.5\,(1 + (L_z - H_b)) \ln(1 + (L_z - H_b)) - 1.5(L_z - H_b))},$$

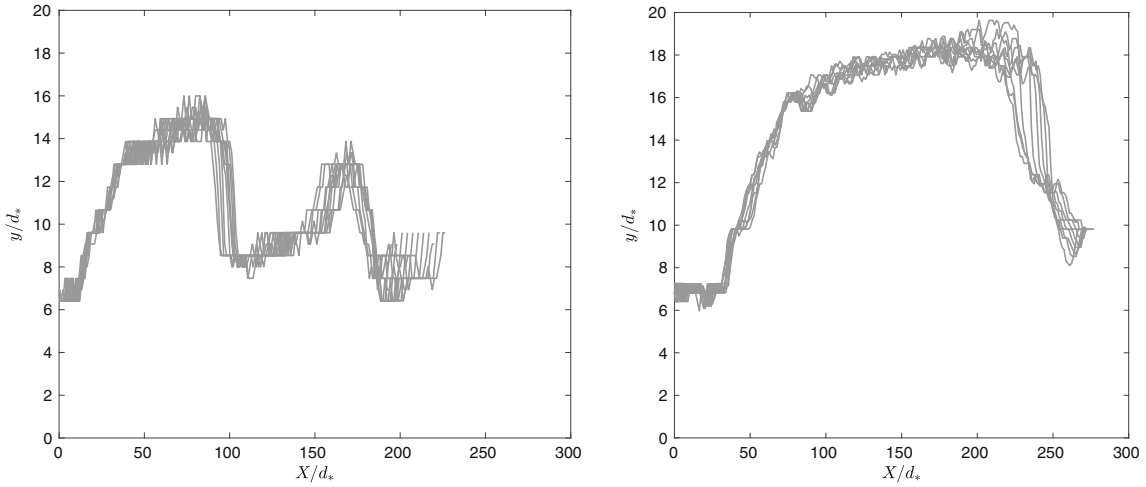

FIGURE 21 River-stream simulation. The surface of the bed when $t^* \in [600,800]$ for $U_b = 0.39$ (m/s) (left) and $U_b = 0.52$ (m/s) (right). The x-axis is the relative longitudinal location $X = (x - u_d t)/d_*$ (x is the horizontal direction, u_d is the migration velocity of the bedform, $K_r = 10^{-6}$ and $\tau_{CR} = 0.05$ (N/m^2)).

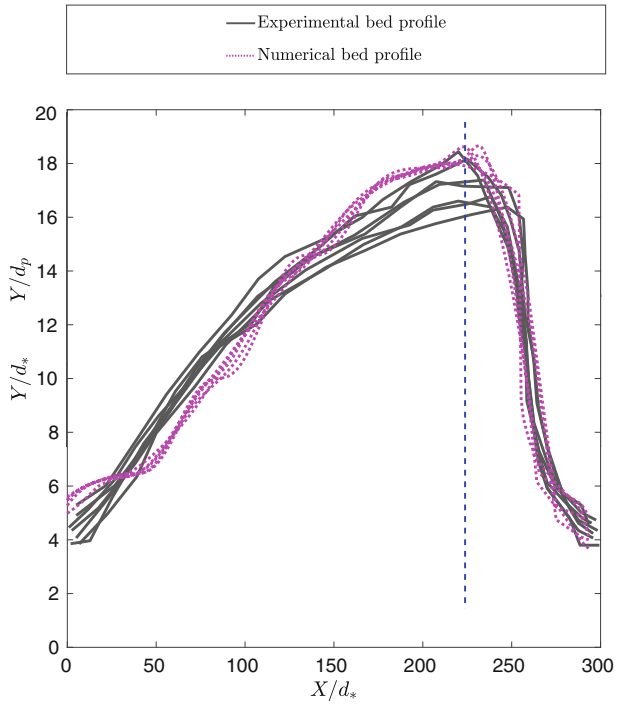

FIGURE 22 River-stream simulation. Bed surface when $t^* \in [600,800]$. The x-axis is the relative longitudinal location $X = (x - u_d t)/d_*$ (x is the horizontal direction, u_d is the migration velocity of the bedform, $K_r = 10^{-6}$ and $\tau_{CR} = 0.05$ (N/m^2)). The vertical solid line in the figure indicates the location of the peak of the bedform. [Colour figure can be viewed at wileyonlinelibrary.com]

where Q is the volumic flow rate, calibrated in order to recover the mean velocity U_b. The discretization considered includes 15,276 elements, 4149 nodes (average size $H = 0.001$), 75,000 cells ($h = 0.0002$) and $\Delta t = 0.0025$ and $\Delta t = 0.002$ respectively. We consider $K_r = 10^{-6}$, a constant shear model with $\tau_{CR} = 0.05$ (N/m^2), $\varepsilon = 10^{-11}$, and $T = 24$ (s). In order to compare with results in Reference 55, we consider the non-dimensional time denoted as $t^* = t/(H_b/U_b)$.

Figure 20 shows snapshots of the sediment profile for the cases of ripples and large dunes, respectively. Note that ripples appear as a result of the shear-induced resuspension. Figure 21 illustrates a further investigation of the stationarity in time of dunes formation for $t^* \in [600,800]$, for these two different regimes. The horizontal axis represents the normalized

relative longitudinal location $X := (x - u_d t)/d_*$, where x is the fixed downstream direction, and u_d is the bedform migration velocity (taken here as $u_d = 0.05$ m/s); snapshots at different time steps are thus overlapping. We can observe that the self-generated bedforms are stationary in time in both regimes.

A comparison of the simulated dune with experimental observations from Reference 55 is done for the case of large dunes (Case 2, $U_b = 0.52$ m/s). Figure 22 displays the averaged experimental bed profile along with the averaged numerical fit ($K_r = 10^{-6}$ and $\tau_{CR} = 0.05$ N/m^2), and shows the close adequation between experimental and numerical wavelengths.

6 | CONCLUSION AND PERSPECTIVES

A three-dimensional numerical model for the transport of sediments within a Newtonian flow with free surfaces has been designed. The numerical method relies on an operator splitting strategy, and an appropriate mix of finite elements, finite volumes, and finite differences methods. Numerical experiments have emphasized the paramount importance of incorporating resuspension effects in scouring and flushing experiments, in particular when there is a shear effect in the flow. Calibration with experimental results has exhibited the flexibility and versatility of the numerical solver. Future perspectives will thus include the extension to poly-disperse sediments and simulations in real-life 3D topographies.

ACKNOWLEDGMENTS

The authors thank Sébastien Boyaval (Laboratoire d'hydraulique Saint-Venant, Université Paris-Est), as the proposed model has emerged from initial discussions with him, within a collaboration in the ANR project ANR-15-CE01-0013. All the computations were performed using the industrial cfsFlow++ software developed by EPFL and Ycoor Systems SA. The authors thank Alexandre Masserey and Julien Hess (Ycoor Systems SA) for implementation support and fruitful discussions. Open access funding provided by Haute Ecole Specialisee de la Suisse Occidentale.

DATA AVAILABILITY STATEMENT

The data that support the findings of this study are available from the corresponding author upon reasonable request.

ORCID

Alexandre Caboussat https://orcid.org/0000-0003-0964-3603
Marco Picasso https://orcid.org/0000-0002-0069-5856

REFERENCES

1. Boillat JL, Pougatsch H. State of the art of sediment management in Switzerland. Proceedings International Workshop and Symposium on Reservoir Sedimentation Management; 2000:35-45.
2. Monaghan JJ, Kos A, Issa N. Fluid motion generated by impact. *J Waterw Port Coast Ocean Eng*. 2003;129(6):250-259.
3. Liu M, Liu GR. Smoothed particle hydrodynamics (SPH): an overview and recent developments. *Arch Comput Meth Eng*. 2010;17:25-76.
4. Ferguson RI, Church M. A simple universal equation for grain settling velocity. *J Sediment Res*. 2004;74(6):933-937.
5. Lyn DA. Resistance in flat-bed sediment-laden flows. *J Hydraul Eng*. 1991;117(1):94-114.
6. Nabian MA, Farhadi L. Multiphase mesh-free particle method for simulating granular flows and sediment transport. *J Hydraul Eng*. 2017;143(4):04016102.
7. Shakibaeinia A, Jin YC. MPS mesh-free particle method for multiphase flows. *Comput Methods Appl Mech Eng*. 2012;229-232:13-26.
8. Capecelatro J, Desjardins O. Eulerian–Lagrangian modeling of turbulent liquid–Solid slurries in horizontal pipes. *Int J Multiphase Flow*. 2013;55:64-79.
9. Shi H, Yu X. An effective Euler-Lagrange model for suspended sediment transport by open channel flows. *Int J Sediment Res*. 2015;30(4):361-370.
10. Finn JR, Li M, Apte SV. Particle based modelling and simulation of natural sand dynamics in the wave bottom boundary layer. *J Fluid Mech*. 2016;796:340-385.
11. Hu HH, Patankar N, Zhu M. Direct numerical simulations of fluid–Solid systems using the arbitrary Lagrangian–Eulerian technique. *J Comput Phys*. 2001;169(2):427-462.
12. Ladd AJC. Numerical simulations of particulate suspensions via a discretized Boltzmann equation. Part 1. Theoretical foundation. *J Fluid Mech*. 1994;271:285-309.
13. Glowinski R, Pan T, Hesla T, Joseph D, Périaux J. A fictitious domain approach to the direct numerical simulation of incompressible viscous flow past moving rigid bodies: application to particulate flow. *J Comput Phys*. 2001;169(2):363-426.
14. Bombardelli F, Jha S. Hierarchical modeling of the dilute transport of suspended sediment in open channels. *Environ Fluid Mech*. 2008;9:207-235.

15. Toorman E. Vertical mixing in the fully developed turbulent layer of sediment-laden open-channel flow. *J Hydraul Eng*. 2008;134(9):1225-1235.
16. Hsu TJ, Jenkins J, Liu PF. On two-phase sediment transport: sheet flow of massive particles. *Proc Royal Soc A Math Phys Eng Sci*. 2004;460(2048):2223-2250.
17. Xin C, Yong L, Xiaojing N, Ming L, Daoyi C, Xiping Y. A general two-phase turbulent flow model applied to the study of sediment transport in open channels. *Int J Multiphase Flow*. 2011;37(9):1099-1108.
18. Michaelides E, Clayton TC, Schwarzkopf JD. *Multiphase Flow Handbook*. 2nd ed. CRC Press; 2016.
19. Chauchat J, Médale M. A three-dimensional numerical model for incompressible two-phase flow of a granular bed submitted to a laminar shearing flow. *Comp Meth App Mech Eng*. 2010;199(9-12):439-449.
20. Nguyen DH, Levy F, Bang DPV, Guillou S, Nguyen KD, Chauchat J. Simulation of dredged sediment releases into homogeneous water using a two-phase model. *Adv Water Resour*. 2012;48:102-112.
21. Ruiz R, Lunati I. Mixed finite element – Discontinuous finite volume element discretization of a general class of multicontinum models. *J Comput Phys*. 2016;322:666-688.
22. Ishi M, Hibiki T. *Thermo-fluid Dynamics of Two-Phase Flow*. Springer; 2010.
23. Zhong D, Wang G, Wu B. Drift velocity of suspended sediment in turbulent open channel flows. *J Hydraul Eng*. 2014;140:35-47.
24. Jha SK, Bombardelli FA. Toward two-phase flow modeling of nondilute sediment transport in open channels. *J Geophys Res Earth*. 2010;115(F3):F03015. doi:10.1029/2009JF001347
25. Boyaval S, Caboussat A, Mrad A, Picasso M, Steiner G. A semi-Lagrangian splitting method for the numerical simulation of sediment transport with free surface flows. *Comput Fluids*. 2018;172:384-396.
26. Caboussat A. A numerical method for the simulation of free surface flows with surface tension. *Comput Fluids*. 2006;35(10):1205-1216.
27. Bonito A, Caboussat A, Picasso M, Rappaz J. A numerical method for fluid flows with complex free surfaces. In: Glowinski R, Neittaanmäki P, eds. *Partial Differential Equations. Volume 16 of Computational Methods in Applied Sciences*. Springer; 2008:187-208.
28. Hirt C. Volume-fraction techniques: powerful tools for wind engineering. *J Wind Eng Ind Aerodyn* 1993; 46-47: 327 - 338. Proceedings of the 1st International on Computational Wind Engineering.
29. Maronnier V, Picasso M, Rappaz J. Numerical SIMULATION OF THREE DIMENSIONAL FREE SURFACE Flows. *Int J Numer Methods Fluids*. 2003;42(7):697-716.
30. Noh WF, Woodward P. SLIC (simple line interface calculation). Proceedings of the 5th International Conference on Numerical Methods in Fluid Dynamics; Vol. 59, 1976:330-340.
31. LeVeque RJ. *Numerical Methods for Conservation Laws. Lectures in MathematicsETH Zurich*. Birkhaüser-Verlag; 1990.
32. Busto S, Ferrín J, Toro E, Vázquez-Cendón M. A projection hybrid high order finite volume/finite element method for incompressible turbulent flows. *J Comput Phys*. 2018;353:169-192. doi:10.1016/j.jcp.2017.10.004
33. Busto S, Dumbser M, Río-Martín L. Staggered semi-implicit hybrid finite volume/finite element schemes for turbulent and non-Newtonian flows. *Mathematics*. 2021;9(22):2972. doi:10.3390/math9222972
34. Río-Martín L, Busto S, Dumbser M. A massively parallel hybrid finite volume/finite element scheme for computational fluid dynamics. *Mathematics*. 2021;9(18):2316. doi:10.3390/math9182316
35. Alvarez M, Gatica GN, Ruiz R. A posteriori error analysis of a fully-mixed formulation for the Brinkman-Darcy problem. *Calcolo*. 2017;54(4):1491-1519.
36. Brinkman HC. A calculation of the viscous force exerted by a flowing fluid on a dense swarm of particles. *Appl Sci Res*. 1949;1:27-34.
37. Ishii M, Zuber N. Drag coefficient and relative velocity in bubbly, droplet or particulate flows. *AICHE J*. 1979;25(5):843-855.
38. Carman P. Fluid flow through granular beds. *Chem Eng Res Des*. 1997;75:S32-S48.
39. Kynch GJ. A theory of sedimentation. *Trans Faraday Soc*. 1952;48:166-176.
40. Helge H, Henrik RN, Aslak T. Maximum principles for a class of conservation laws. *SIAM J Appl Math*. 1995;55(3):651-661.
41. Blom G, Aalderink RH. Calibration of three resuspension/sedimentation models. *Water Sci Technol*. 1998;37(3):41-49.
42. Filostrat JE. *Estimation of Sediment Resuspension and Deposition in Coastal Waters*. PhD thesis. University of New Orleans, New Orleans; 2014.
43. van Rijn LC. *Principles of Sediment Transport in Rivers, Estuaries and Coastal Seas*. Lectures in Mathematics Universitet Utrech. Aqua Publications; 1993.
44. Lamb MP, Dietrich WE, Venditti JG. Is the critical shields stress for incipient sediment motion dependent on channel-bed slope? *J Geophys Res*. 2008;113:F02008.
45. Torok GT, Joza J, Baranya S. A shear Reynolds number-based classification method of the non-uniform best load transport. *Watermark*. 2019;11:73.
46. Pironneau O, Liou J, Tezduyar T. Characteristic-Galerkin and Galerkin/least-squares space-time formulations for the advection-diffusion equation with time-dependent domain. *Comput Methods Appl Mech Eng*. 1992;100:117-141.
47. Wang H, Dahle H, Ewing R, Espedal M, Sharpley R, Man S. An ELLAM scheme for advection-diffusion equations in two dimensions. *SIAM J Sci Comput*. 1999;20:2160-2194.
48. Caboussat A, Clausen P, Rappaz J. Numerical simulation of two-phase flow with interface tracking by adaptive eulerian grid subdivision. *Math Comput Model*. 2012;55:490-504.
49. Caboussat A, Picasso M, Rappaz J. Numerical simulation of free surface incompressible liquid flows surrounded by compressible gas. *J Comput Phys*. 2005;203(2):626-649.
50. Arnold D, Brezzi F, Fortin M. A stable finite element for the stokes equations. *Calcolo*. 1984;21(4):337-344.

51. Franke R. Scattered data interpolation: test of some methods. *Math Comput*. 1982;38:181-200.
52. Kusuma J, Ribal A, Mahie A. On FTCS approach for box model of three-dimension advection-diffusion equation. *Int J Differ Equ*. 2018;2018:1-9.
53. Manenti S, Sibilla S, Gallati M, Agate G, Guiandalini R. SPH simulation of sediment flushing induced by a rapid water flow. *J Hydraul Eng*. 2012;138:272-284.
54. Khanpour M, Zarrati A, Kolahdoozan M, Shakibaeinia A, Amirshahi M. Mesh-free SPH modeling of sediment scouring and flushing. *Comput Fluids*. 2016;129;67-78.
55. Rui S, Heng X, Kyle S. Particle dynamics in self-generated dunes over a range of hydraulic and sediment transport conditions using LES–DEM. arXiv e-prints, 2016.
56. Kidanemariam AG, Uhlmann M. Interface-resolved direct numerical simulation of the erosion of a sediment bed sheared by laminar channel flow. *Int J Multiphase Flow*. 2014;67:174-188.
57. Rui S. Sediment micromechanics in sheet flows induced by asymmetric waves: a CFD-DEM study. *Comput Geosci*. 2016;96:35-46.

How to cite this article: Mrad A, Caboussat A, Picasso M. A splitting method for the numerical simulation of free surface flows with sediment deposition and resuspension. *Int J Numer Meth Fluids*. 2022;1-20. doi: 10.1002/fld.5122